

# Effects of Al-Si Coating and Zn Coating on the Hydrogen Uptake and Embrittlement of Ultra-High Strength Press-Hardened Steel

Kyoung Rae Jo<sup>a</sup>, Lawrence Cho<sup>a,b,\*</sup>, Dimas H. Sulistiyono<sup>a</sup>, Eun Jung Seo<sup>a,c</sup>,  
Seong Woo Kim<sup>d</sup>, Bruno C. De Cooman<sup>a,†</sup>

<sup>a</sup>Graduate Institute of Ferrous Technology, Pohang University of Science and Technology,  
Pohang, 37673, South Korea

<sup>b</sup>National Institute of Standards and Technology, Boulder, CO 80305, USA

<sup>c</sup>Advanced Steel Processing and Products Research Center,  
Colorado School of Mines, Golden, CO 80401, USA

<sup>d</sup>Technical Research Laboratories, POSCO, Gwangyang, 57807, South Korea

<sup>†</sup>This paper is dedicated to the memory of our co-author, Bruno C. De Cooman, who passed  
away on August 29, 2018.

\*Corresponding author. Tel: +1-303-497-6853. Email: [lawrence.cho@nist.gov](mailto:lawrence.cho@nist.gov)

## Abstract

Press-hardened steel (PHS), used for automotive safety-related structure parts, is sensitive to hydrogen embrittlement due to its martensitic microstructure. Hydrogen is introduced in PHS during the hot press forming (HPF) process, by an atmospheric corrosion process. In this study, the hydrogen embrittlement behavior of uncoated, aluminized, and galvanized PHSs was investigated. The Al-10%Si coating promoted the absorption of diffusible hydrogen at elevated temperature during the HPF while the reacted coating layer prevented the absorbed hydrogen from out-diffusing through the reacted coating surface layer at room temperature. Therefore, the aluminized PHS showed a greater sensitivity to both the hydrogen uptake and the resultant embrittlement, as compared to the uncoated and galvanized PHSs. Use of galvanized PHS for HPF application reduces the risk of hydrogen embrittlement, since the Zn coating effectively prevents

the hydrogen uptake. The greater embrittlement resistance of the galvanized PHS is possibly due to the inhibition of the hydrogen generation reaction by the surface ZnO oxide layer and the low rate of hydrogen transport through the liquid Zn phase.

**Keywords:** Zn coating; Al-Si coating; press-hardened steel; martensite; hydrogen embrittlement; hot press forming.

## Highlights

- Aluminized press hardened steel is most susceptible to the H uptake and embrittlement.
- The H-induced loss of the plasticity is more pronounced at low strain rates.
- H atoms absorbed in the coated steel are trapped mostly in the martensitic matrix.
- Zn coating effectively prevents the H uptake during hot press forming.
- Coating-type dependent H absorption and desorption mechanisms are proposed.

## 1 Introduction

Press-hardened steels (PHSs) are used more frequently for automotive body-in-white design because of increased requirements related to safety standards and weight reduction in the automotive industry. The PHS parts for automotive applications are produced by hot press forming (HPF), a process also known as hot stamping [1]. In the direct HPF process, a blank cut from a cold-rolled and continuously annealed steel sheet is heated at 900-950 °C for a duration ranging from 3-10 min to attain a fully austenitic microstructure, which is a favorable material condition for the forming operations. The blank is then simultaneously press-formed and quenched in water-cooled quenching dies to obtain a high strength, martensitic microstructure. The application of the HPF process enables to produce spring back-free ultra-high strength steel parts [2]. The hardenable 22MnB5 steel having an ultimate tensile strength (UTS) of approximately 1500 MPa in the press-hardened state, is most commonly used for the HPF process. More recently, efforts have been made to increase the tensile strength of PHS towards 2000 MPa, in order to further reduce vehicle weight through the use of thinner steel sheets [2].

Metallic coatings such as Al-Si coatings [3] and Zn-based coatings [4] have been used to protect PHS parts from various types of corrosion. An uncoated PHS is significantly oxidized, and the sheet surface is decarburized during the austenitization stage of the HPF process. The oxide scale formed at the steel surface is usually removed by shot blasting [5]. The shot blasting process can be omitted when the PHS is protected with a metallic coating [5]. To date, the Al-10%Si coating is the most widely used coating for PHS in HPF applications. Pure Zn coatings, which can provide cathodic corrosion protection, are also used as a coating system for PHS. Zn-assisted liquid-metal-embrittlement (LME) during the HPF process of Zn-coated PHS has, however, been reported [6].

Previous studies have shown that PHS is sensitive to hydrogen uptake, which introduces potential risks associated with hydrogen embrittlement [7-10]. The PHS absorbs hydrogen during the austenitization stage in the HPF process. The source of hydrogen is the moisture in the annealing furnace [7-10]. This hydrogen uptake can cause a severe degradation of the mechanical properties, i.e. strength, ductility, toughness, and bendability, of the PHS, since martensitic microstructure has

a high sensitivity to hydrogen-induced cracking [7-10]. The susceptibility to hydrogen embrittlement increases with increasing strength in PHSs [11].

Several investigations have focused on hydrogen permeation through coatings at room temperature [12-14]. In general, coatings act as a barrier to hydrogen ingress to the steel substrate at room temperature. Typically, aluminizing of steels has been used as an effective method to prevent the ingress of hydrogen at room temperature [12] because the room temperature diffusivity of hydrogen in Al is very low ( $10^{-11}$ - $10^{-15}$   $\text{m}^2 \text{s}^{-1}$  [12, 15]). While Zn coating can also suppress the hydrogen ingress into steel [13, 14], the mechanism is clearly different from that of Al-based coatings. Interestingly, hydrogen diffuses comparatively fast in pure Zn in the solid state at room temperature ( $\sim 10^{-8}$   $\text{m}^2 \text{s}^{-1}$  [16]). Jeon et al. [13] reported that the suppression of hydrogen permeation by the Zn coating was associated with the formation of a Zn passive film at the surface, leading to a decrease of the hydrogen evolution rate. On the other hand, the coatings may also act as an obstacle to hydrogen out-diffusion once the steel has absorbed hydrogen. Therefore, an unfavorable combination of thermodynamic properties, hydrogen solubility, and hydrogen diffusivity of a coating system may promote hydrogen embrittlement.

Comparatively, there is limited information in the literature with respect to interactions between coated steels and hydrogen at *elevated* temperatures; in particular, it is still unclear whether a Zn coating on steels stimulates or suppresses hydrogen uptake at elevated temperatures. Furthermore, influences of the coating and surface microstructures on the hydrogen uptake and resulting embrittlement of ultra-high strength PHS have not been studied systematically. The present study focused on the time-dependent hydrogen embrittlement behavior for uncoated, aluminized, and galvanized 2000 MPa PHSs produced by HPF. The influences of the coating type on hydrogen absorption and desorption of the PHSs were investigated by means of hydrogen thermal desorption analysis (TDA). Uni-axial tensile testing was employed to evaluate the severity of the hydrogen effect on the mechanical properties of the uncoated and coated PHSs. Mechanisms describing the hydrogen absorption and desorption behavior of uncoated and coated PHSs were also proposed.

## **2 Experimental procedures**

### **2.1 Materials and HPF simulation**

Uncoated, aluminized (Al-10 wt. % Si coated), and galvanized (pure-Zn coated) 35MnB5 steel grades were used in the present study. 10-20 ppm B was added to the steel composition to enhance their hardenability. The formation of BN was avoided by addition of 0.03 wt. % Ti, which stabilizes N as TiN [17]. The uncoated PHS was produced from cold-rolled, full hard steel continuously annealed at 800 °C. The thickness of the cold-rolled sheet was 1.5 mm. The aluminized PHS was produced by means of hot-dip-aluminizing in an Fe-saturated Al-10 wt. % Si bath at 680 °C. The Zn-coating was applied by means of hot-dip-galvanizing in an Fe-saturated Zn-0.22 wt. % Al bath at 460 °C. The thicknesses of the Al-Si coating and Zn coating were approximately 30 μm and 10 μm, respectively, which are in the range of typical coating thicknesses for automotive steels.

For the HPF simulation, the uncoated and coated PHSs were first heated to an austenitizing temperature of 900 °C and isothermally held for 6 min to 50 min in an electrically-heated furnace. The specimens were then transferred to a laboratory HPF simulator and quenched between water-cooled dies to room temperature. Pressurized air was used to eliminate the surface oxide scale of the uncoated PHS. In the actual industrial process, the scale removal is generally accomplished by shot blasting. The present study did not utilize “conventional” hydrogen charging methods such as electrolytic charging and gaseous charging. Instead, the PHS absorbed hydrogen naturally during the austenitization treatment of the HPF process, by the reaction between the metal surface and water vapor in the furnace atmosphere as will be discussed in section 3.4. The details of the laboratory HPF simulator and hydrogen charging procedures are fully described elsewhere [10, 11].

## 2.2 Microstructural analysis

The microstructure, constituent phases, and chemistries of the steel substrate and reacted coating layer of the PHS specimens after the HPF simulation were investigated by means of field emission-scanning electron microscopy (SEM), electron backscatter diffraction (EBSD), field emission-electron probe microanalysis (EPMA), and glow discharge optical emission spectroscopy (GDOES). Prior to the microstructural analysis, the cross sections of the specimens after the HPF simulation were mechanically ground and polished. A final polishing step was performed using colloidal silica with a particle size of 0.06  $\mu\text{m}$ . The SEM, EBSD, and EPMA analyses were performed on the through-thickness plane with the transverse direction of the rolled sheet being perpendicular to the polish plane. The EPMA was operated at 15 keV using a 50 nA beam current. Chemical concentration-depth profiles of the surface of the aluminized and galvanized PHS specimens were obtained by GDOES, operated at a voltage of 700 V and a constant current of 30 mA. The analyzed area was approximately 4 mm in diameter.

### **2.3 TDA and mechanical testing**

TDA was conducted immediately after the HPF simulation and after aging at room temperature for one week. TDA was performed using a diffusible hydrogen analyzer equipped with a thermal conductivity detector. The specimens for the TDA were 1.5 mm in thickness, 20 mm in width, and 100 mm in length. The hydrogen desorption rate for the uncoated and aluminized PHS specimens after the HPF simulation was measured during heating from 50 °C to 800 °C using a heating rate of 20 °C/min. The carrier gas was pure N<sub>2</sub>. In the case of the galvanized PHS specimen, the TDA was performed below 400 °C, i.e. below the melting temperature of Zn, in order to avoid the contamination associated with Zn evaporation, of the detector of the TDA instrument.

Uni-axial tensile tests were conducted immediately after the HPF simulation and after aging at room temperature for one week. Uni-axial tensile tests using ASTM E8 standard-sized tensile specimens were performed using a strain rate ranging from  $5 \times 10^{-5} \text{ s}^{-1}$  to  $5 \times 10^{-2} \text{ s}^{-1}$ . For selected conditions, the fracture surface of the tensile specimens was analyzed in a 3D digital optical microscope and SEM.

### 3 Results and discussion

#### 3.1 Microstructure and chemistry of the reacted coating layer and steel substrate

Figure 1 shows SEM micrographs and EBSD results of the cross-sections of the uncoated, aluminized, and galvanized PHSs, austenitized at 900 °C for an austenitizing time of 6 min and die-quenched to room temperature for the HPF simulation. The uncoated PHS had a fully martensitic microstructure (figure 1(a)). In the case of the aluminized PHS, the austenitization treatment causes chemical reactions between the Al-10%Si coating and the steel substrate, which create the complex multi-layered microstructure near the surface (figure 1(b)). The microstructure of the reacted coating layer of the aluminized PHS consisted mainly of the  $\text{Fe}_2\text{Al}_5$  phase. In the  $\text{Fe}_2\text{Al}_5$  layer, there were Fe-Al-Si intermetallic constituents that could not be detected by means of EBSD (marked by the white arrows in the phase map in figure 1(b)). The Fe-Al-Si intermetallic constituents were present mainly along the grain boundaries of the  $\text{Fe}_2\text{Al}_5$  phase. The Fe-Al-Si intermetallic phase is likely an  $\text{Al}_2\text{Fe}_3\text{Si}_3$  ( $\tau_1$ ) phase according to a previous study by Windmann et al. [18]. Iron aluminide, FeAl, having an ordered B2 structure [19] often formed as islands next to the  $\tau_1$  phase (figure 1(b)). Note that the regions of the ordered B2 crystal structure could not be differentiated from those of the BCC crystal structure by the EBSD technique because of the close relationships between the two crystal structures, i.e. the B2 structure is an ordered structure based on the BCC lattice [19]. The co-precipitation of the  $\tau_1$  and FeAl phases at the grain boundaries of the  $\text{Fe}_2\text{Al}_5$  phase is associated with the low solubility of Si in  $\text{Fe}_2\text{Al}_5$  phase (approximately 6 at.-%) [18]. A layer of bcc solid solution of Al and Si in  $\alpha$ -Fe,  $\alpha$ -Fe(Al,Si), was present at the coating/substrate interface. The  $\alpha$ -Fe(Al,Si) layer was formed by the diffusion of Al and Si, both strong ferrite stabilizers, into the austenite during the austenitization treatment. The steel matrix below the  $\alpha$ -Fe(Al,Si) layer displayed lath martensitic microstructure.

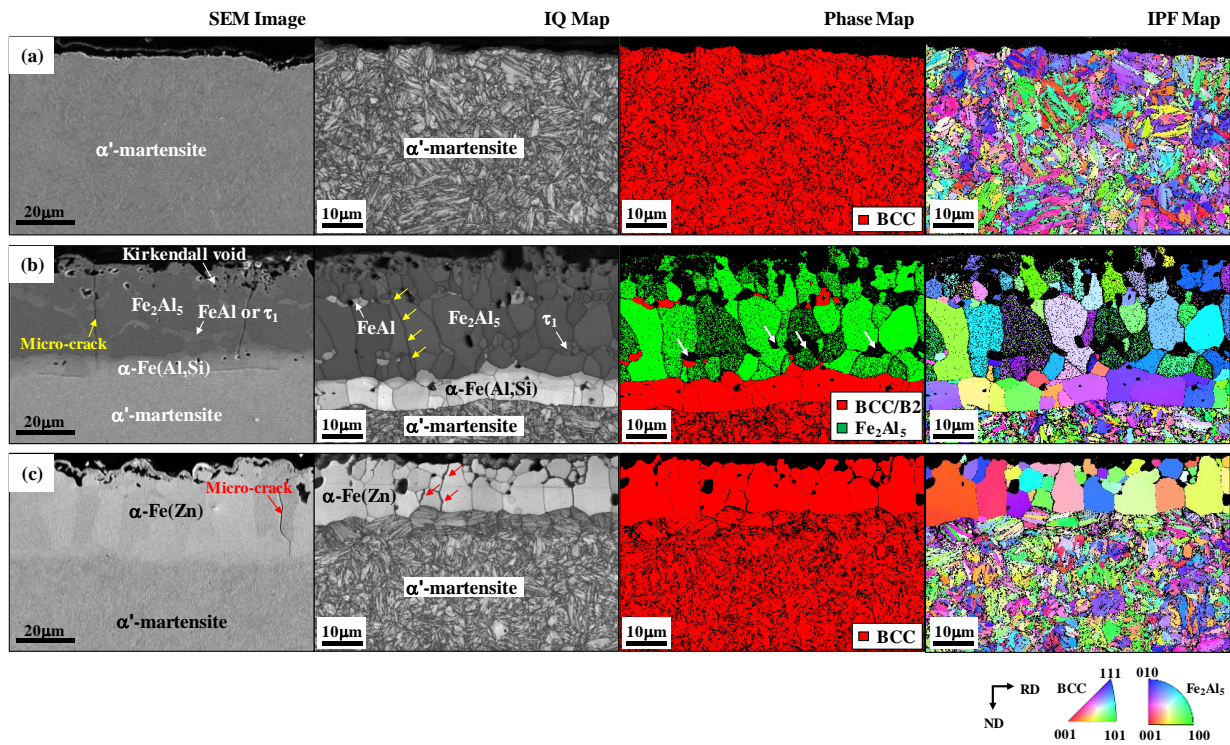


Fig. 1 Cross-sectional SEM micrographs and EBSD results of the surface and subsurface of (a) the uncoated, (b) aluminized, and (c) galvanized PHSs after the HPF simulation. In the first column, SEM micrographs are shown. EBSD image quality (IQ) maps, phase maps, and inverse pole figure (IPF) maps are shown in the second, third, and fourth columns, respectively. In the phase maps, red corresponds to bcc crystal structures ( $\alpha'$  martensite,  $\alpha$ -Fe(Al,Si), and  $\alpha$ -Fe(Zn)) or ordered B2 crystal structure (FeAl) and green corresponds to  $\text{Fe}_2\text{Al}_5$  phase. In all cases, the specimens were austenitized at 900 °C for 6 min prior to the die-quenching for the HPF simulation.

The reacted coating layer of the galvanized PHS consisted mainly of a bcc solid solution of Zn in  $\alpha$ -Fe,  $\alpha$ -Fe(Zn). The  $\alpha$ -Fe(Zn) layer was formed by the reaction of Zn and Fe during the austenitization treatment (figure 1(c)). Fe-Zn intermetallic phases, such as the  $\Gamma$ - $\text{Fe}_3\text{Zn}_{10}$  phase, may be formed in the reacted coating layer on galvanized PHSs depending on the austenitizing conditions [20]. No intermetallic phase was detected in the EBSD analysis of the present study (figure 1(c)). A fully martensitic microstructure is clearly visible below the reacted coating layer.  $\alpha$ -Fe(Zn) phase and Fe-Zn intermetallic phases are brittle [21], similar to Fe-Al intermetallic phases formed in the aluminized PHS.

The microstructure and phases at the surface and in the subsurface of the PHSs were also analyzed by EPMA (figure 2) and GDOES (figure 3) analysis. Figure 2 shows SEM micrographs and corresponding EPMA elemental maps of the cross-sections of the uncoated, aluminized, and galvanized PHSs after the HPF simulation. The oxygen concentration detected at the surface of the uncoated PHS was rather small (figure 2(a)) since the surface oxide scale was removed by the high-pressure air after the HPF. At the top surface of the aluminized PHS (figure 2(b)), a thin layer with a high oxygen content, which was mainly an Al oxide layer, was present. In the reacted coating layer of the aluminized PHS (figure 2(b)), islands of the  $\tau_1$  and FeAl phases embedded in the  $\text{Fe}_2\text{Al}_5$  layer are characterized by the higher contents of Fe and Si and the lower content of Al compared to the  $\text{Fe}_2\text{Al}_5$  phase, as indicated by the dashed circle in figure 2(b). The Al and Si diffusion layer,  $\alpha\text{-Fe}(\text{Al},\text{Si})$  layer, at the coating/substrate interface is clearly visible in the EPMA mapping results of figure 2(b). The galvanized PHS had a surface oxide layer (figure 2(c)). The oxide layer on the galvanized PHS comprises of ZnO and  $\text{Al}_2\text{O}_3$  according to the previous study by Lee et al. [22]. Note that Al is usually present as a  $\text{Fe}_2\text{Al}_5$  inhibition layer at the coating/substrate interface of as-hot dip galvanized steels. The Al diffuses to the coating surface to form an  $\text{Al}_2\text{O}_3$  layer during the austenitization stage of the HPF process [22], which is responsible for the absence of Al near the coating/substrate interface after the HPF (figure 2(c)). The Zn concentration in the  $\alpha\text{-Fe}(\text{Zn})$  layer of the reacted coating layer of the galvanized PHS ranged from 25.4 wt. % to 26.3 wt. % (figure 2(c)). No evidence of Fe-Zn intermetallic phases was found in the EPMA results, which is consistent with the EBSD results shown in figure 1(c).

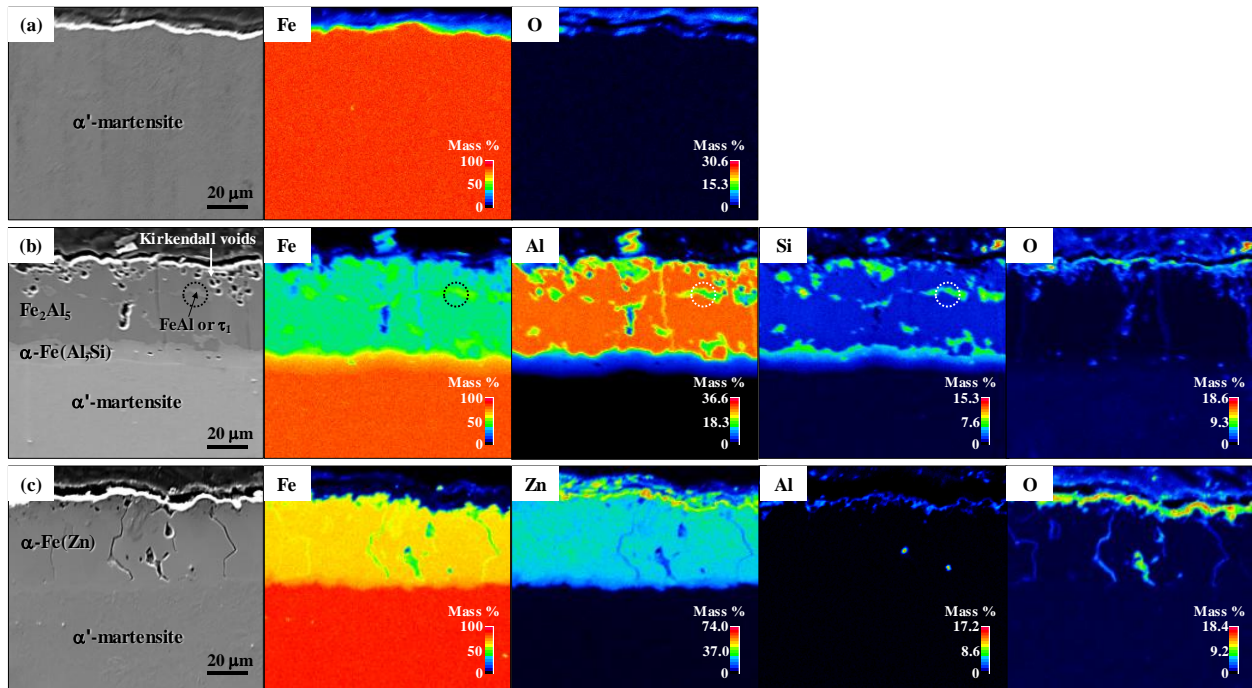


Fig. 2 Cross-sectional SEM micrographs and the EPMA elemental mapping results of the surface and subsurface of (a) the uncoated, (b) aluminized, and (c) galvanized PHSs after the HPF simulation. Elemental mapping images for Fe and O are shown in (a). Elemental mapping images for Fe, Al, Si, and O are shown in (b). Elemental mapping images for Fe, Zn, Al, and O are shown in (c).

It is important to note that micro-cracks were frequently observed in the reacted coating layer of both the aluminized and galvanized PHSs. Micro-cracks were visible in the  $\text{Fe}_2\text{Al}_5$  grains of the reacted coating layer of the aluminized PHS (figures 1(b) and 2(b)). The path of a transgranular micro-crack is indicated by the yellow arrows in the image quality (IQ) map in figure 1(b). The micro-cracks were formed by thermal stresses due to differences in the thermal expansion coefficient of the different phases during the solidification and transformation of the coating layer. In addition, Fe-Al intermetallic crystals are known to be brittle [23], and thus the cracks could also be formed by the mechanical stresses applied during the die-quenching. Kirkendall voids, formed due to the significant difference in the diffusion coefficients of Fe and Al in the Fe-Al intermetallics [24], were also visible in the reacted coating layer (figures 1(b) and 2(b)). The densities of the micro-crack and Kirkendall void in the reacted coating layer of an aluminized PHS are affected by the austenitizing conditions, i.e. the micro-crack and void densities generally decrease with increasing austenitizing temperature or austenitizing time [18]. The reacted coating

layer of the galvanized PHS also contained micro-cracks, similar to those in the aluminized PHS (marked by the red arrows in figure 1(c)).

The effect of the austenitizing time on the composition and thickness of the reacted coating layers of the aluminized and galvanized PHSs was studied by means of GDOES (figure 3). The thickness of the reacted coating layer for each condition was determined by measuring the depth at which the elemental concentrations reach the nominal steel compositions, as indicated by the dashed lines in figures 3. For the aluminized PHS (figures 3(a) to (c)), the thickness of the reacted coating layer increased with increasing austenitizing time. In addition, an increase of the austenitizing time resulted in a slight increase of the thickness of the Al oxide layer of the aluminized PHS. Temperature- and time-dependent phase evolution in the Al-Si coating on a PHS during the austenitization stage in HPF process has been investigated in detail by Windmann et al. [18]. An extension of the austenitizing time results in more reactions between Al and Si in the coating and Fe of the steel substrate, leading to a change of the major constituent in the reacted coating from  $\text{Fe}_2\text{Al}_5$  to  $\text{FeAl}$  phase [18]. Similarly, the thicknesses of the surface oxide layer and reacted coating layer of the galvanized PHS were increased with increasing austenitizing time (figures 3(d) to (f)). The thickening of the oxide layer was more significant for the galvanized PHS, as compared to the aluminized PHS. The Zn content in the  $\alpha\text{-Fe}(\text{Zn})$  layer of the reacted coating layer was close to 20 at.-%, independent of the austenitizing time. This value is much lower than the maximum solubility of Zn in  $\alpha\text{-Fe}$  at the austenitizing temperature of 900 °C, i.e. 31.9 at.-% Zn, supporting the EBSD and EPMA results that no Fe-Zn intermetallic phase was present in the reacted coating layer of the galvanized PHS.

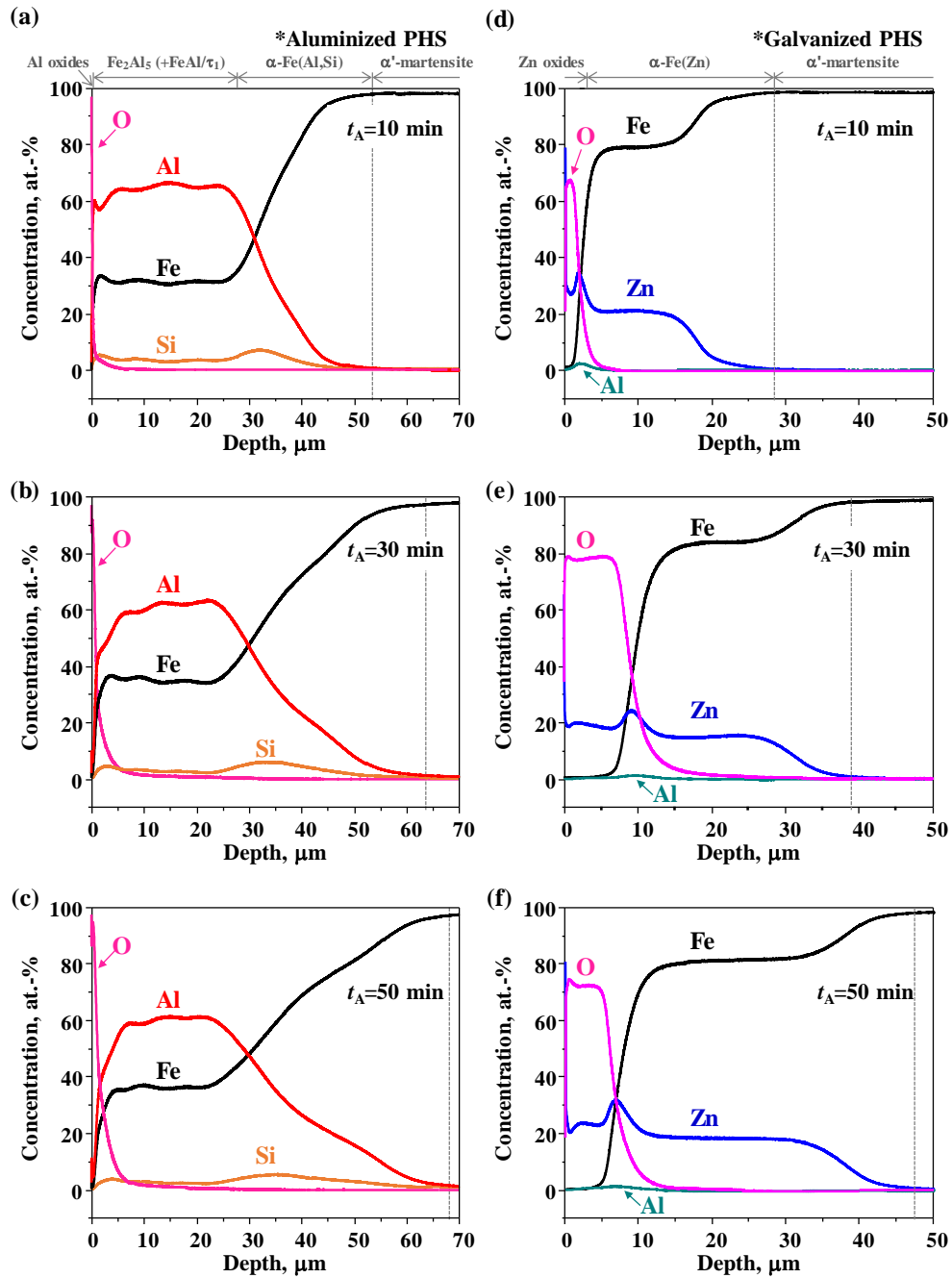


Fig. 3 GDOES concentration-depth profiles for the aluminized PHS ((a) to (c)) and galvanized PHS ((d) to (f)), austenitized at 900 °C for an austenitizing time ( $t_A$ ) in the range of 10-50 min and die-quenched to room temperature.

### 3.2 Influence of coating type on the kinetics of hydrogen absorption and desorption

Figures 4 and 5 show the hydrogen-TDA results for the uncoated, aluminized, and galvanized PHSs austenitized at 900 °C for an austenitizing time in the range of 6-50 min. Figure 4(a) shows the representative TDA curves for the PHSs austenitized at 900 °C for 6 min. A hydrogen-desorption-rate peak was clearly observed in the temperature range of 100 to 300 °C in the TDA curve of the uncoated PHS (figure 4(a)). This low-temperature peak is labeled “Peak 1” in figure 4(a). The temperature of the peak maximum of Peak 1 was found at approximately 200 °C. The characteristics of the hydrogen-desorption-rate peaks observed in the present study have been thoroughly investigated in a recent study by the present authors [10]. The value of the activation energy obtained from Peak 1 was 22.1 kJ/mol [10]. Peak 1 is associated with hydrogen atoms trapped in the stress field surrounding dislocations. A second hydrogen-desorption-rate peak, labeled “Peak 2” in figure 4(a), was observed at approximately 500 °C in the TDA curve of the uncoated PHS (figure 4(a)). The value of the activation energy obtained from Peak 2 was 74.7 kJ/mol, and this peak is related to hydrogen-trapping at the dislocation cores [10]. A third hydrogen-desorption-rate peak, labeled “Peak 3”, was seen at approximately 720 °C in the TDA curve of the uncoated PHS (figure 4(a)). The origin of Peak 3 is unclear, because Peak 3 appeared occasionally in the TDA curves, i.e. Peak 3 was not reproducible. It is interpreted that Peak 3 is part of Peak 2, associated with hydrogen-trapping in the dislocation cores. Further details about potential hydrogen traps in martensitic steels and interpretation of the TDA results have been reported in a previous study [10].

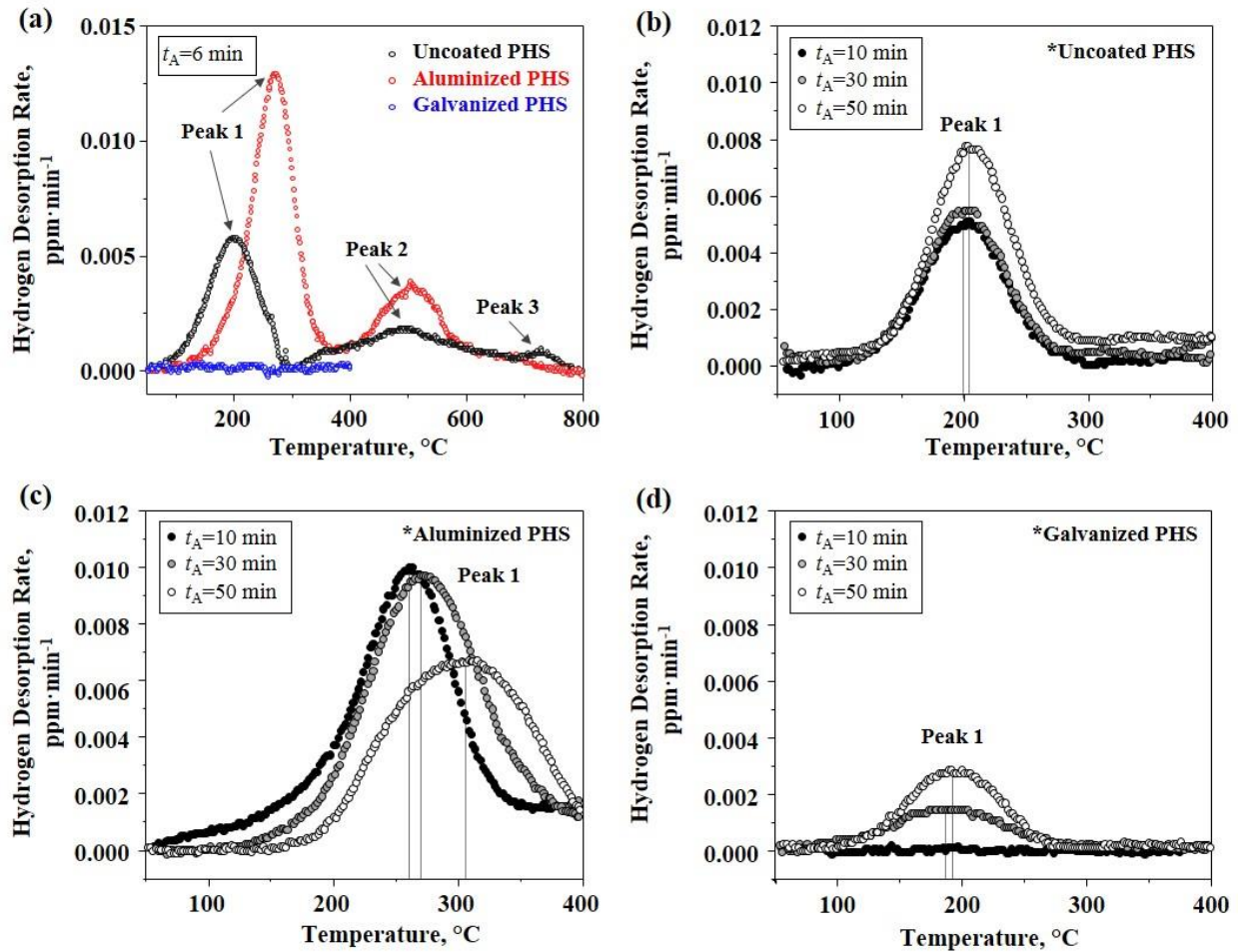


Fig. 4 TDA curves for the uncoated, aluminized, and galvanized PHSs, austenitized at 900 °C for an austenitizing time ( $t_A$ ) in the range of 6-50 min and die-quenched to room temperature. (a) Comparison of the TDA curves for the uncoated, aluminized, and galvanized PHSs. (b) Changes in the TDA curves of (a) the uncoated, (b) aluminized, and (d) galvanized PHSs with increasing hold time. In all cases, TDA was done immediately after the HPF simulation. The TDA heating rate was 20 °C/min.

In the TDA curve of the aluminized PHS (figure 4(a)), three hydrogen-desorption-rate peaks were also detected. They occurred at higher temperatures, compared to the corresponding peaks for the uncoated PHS. The shift of the hydrogen-desorption-rate peaks was caused, most likely, by the presence of the Al coating, *i.e.* diffusion of hydrogen in solid Al is very slow [25] and thus, the Al coating slows down the desorption process of hydrogen trapped at the martensitic matrix during the TDA. The integrated intensities of the hydrogen-desorption-rate peaks were higher for the aluminized PHS as compared to the uncoated PHS (figure 4(a)), indicating that the aluminized

PHS absorbed more hydrogen. No hydrogen-desorption-rate peak was noted in the TDA curve of the galvanized PHS austenitized at 900 °C for 6 min (figure 4(a)). Note that for the galvanized specimen, the TDA was performed below 400 °C to avoid the Zn-vapor-associated contamination of the detector of the TDA instrument.

“Diffusible hydrogen” denotes the solute hydrogen in the lattice and the hydrogen weakly trapped at reversible trapping sites, which play a crucial role in hydrogen-induced cracking [26]. In the present study, the diffusible hydrogen is defined as the hydrogen that desorbs at low temperature, which corresponds to the hydrogen atoms which give rise to Peak 1 in the TDA curves. Figures 4(b) to (d) show the evolution of the low-temperature hydrogen-desorption-rate peak (Peak 1) in the TDA curves of the PHSs as a function of the austenitizing time. The TDA curves of the uncoated PHS (figure 4(b)) exhibit that the intensity of Peak 1 increased with increasing austenitizing time. In the TDA curve of the aluminized PHS (figure 4(c)), as the austenitizing time increased, the maximum intensity of Peak 1 decreased while Peak 1 was broadened and shifted to higher temperature. The broadening and shift of Peak 1 are very likely associated with the thickening of the reacted coating layer, in which hydrogen diffusion is slow. As the austenitizing time extended from 10 min to 50 min, the thickness of the reacted coating layer, estimated based on the GDOES results (figure 3(c)), was increased from 28  $\mu\text{m}$  to 68  $\mu\text{m}$ . A similar peak shift was noted for the uncoated and galvanized PHSs (figures 4(b) and (d)), but the extent of the peak shift was insignificant compared to the aluminized PHS. Kuhlmann et al. [29] reported that the kinetics of hydrogen desorption of an uncoated press hardened 22MnB5 steel were comparable to those of a Zn-coated press hardened 22MnB5 steel at room temperature, i.e. the reacted coating layer of the Zn-coated PHS had no significant impact on the kinetics of the hydrogen desorption. However, hydrogen desorption from a hydrogen-charged aluminized PHS was extremely slow compared to an uncoated PHS [29], which explains the significant peak shift with increasing coating thickness noted for the aluminized PHS (figure 4(c)).

In the TDA curves of the galvanized PHS, a hydrogen-desorption-rate peak (Peak 1) started to appear when the austenitization time was 30 min (figure 4(d)). Possible mechanisms of this

delayed appearance of the hydrogen-desorption-rate peak will be discussed in section 3.4 on the basis of the kinetics of hydrogen generation and transport.

Figure 5(a) shows the TDA results for the evolution of the diffusible hydrogen content of the PHSs austenitized at 900 °C for an austenitizing time in the range of 6-50 min. The diffusible hydrogen content for each PHS was determined by integration of Peak 1 in the TDA curves. The hydrogen content after the HPF simulation was significantly influenced by the coating type or surface status. The uncoated PHS contained about 0.10 ppm of diffusible hydrogen after an austenitizing time of 6 min. Note that a time duration of 6 min is close to the typical austenitizing time of the industrial HPF process. The diffusible hydrogen content of the uncoated PHS increased only slightly, i.e. to 0.15 ppm, for an austenitizing time of 50 min. A much higher diffusible hydrogen content was present in the aluminized PHS, i.e. the presence of an Al-rich coating on the PHS promoted the hydrogen uptake. The diffusible hydrogen content of the aluminized PHS was 0.28 ppm after an austenitizing time of 6 min. This value is similar to the hydrogen content of an aluminized 22MnB5 PHS after the HPF process, i.e. 0.35 ppm, reported by Georges et al. [7]. The diffusible hydrogen content was slightly higher, i.e. 0.32 ppm, when the austenitizing time was increased to 50 min. Unlike the Al-10%Si coating, the Zn-coating effectively prevented the hydrogen uptake of the PHS. No diffusible hydrogen was detected in the galvanized PHS after an austenitizing time of 6 min. The diffusible hydrogen content increased to 0.06 ppm for an austenitizing time of 50 min.

It is well known that an increase in the austenitizing time results in an increase in the sizes of prior austenite grain and martensite substructure of a PHS, leading to a decrease of the area of grain and lath boundaries. Therefore, a longer austenitizing time and the resulting decreased hydrogen trapping sites may cause a slightly decreased hydrogen uptake of a PHS. The effect of the substrate microstructure, i.e. a drop in the diffusible hydrogen content with increasing austenitizing time, was however not noted in the TDA results (figure 5(a)), which implies that the hydrogen absorption mechanisms for the PHSs were controlled mainly by the surface status or coating type rather than the microstructure of the steel matrix

In order to investigate the difference in the hydrogen desorption behavior between the PHSs, the specimens after the HPF were aged at room temperature for one week prior to TDA. Figure 5(b) shows the diffusible hydrogen content for each PHS before and after the room temperature aging. The diffusible hydrogen content of the uncoated PHS decreased to 0.001 ppm, i.e. most of the hydrogen diffused out of the uncoated PHS within a week. The initial hydrogen content of the aluminized PHS of 0.28 ppm decreased by half, to 0.14 ppm after one week. A considerable amount of diffusible hydrogen was, therefore, still present in the aluminized PHS after the one-week aging. It is known from previous studies [30, 31] that metallic or inorganic surface layers can act as a diffusion barrier for hydrogen out-diffusion at room temperature. This appears to be the case for the aluminized PHS. In the case of the galvanized PHS, the initial diffusible hydrogen content was extremely small, and remained so after the aging step.

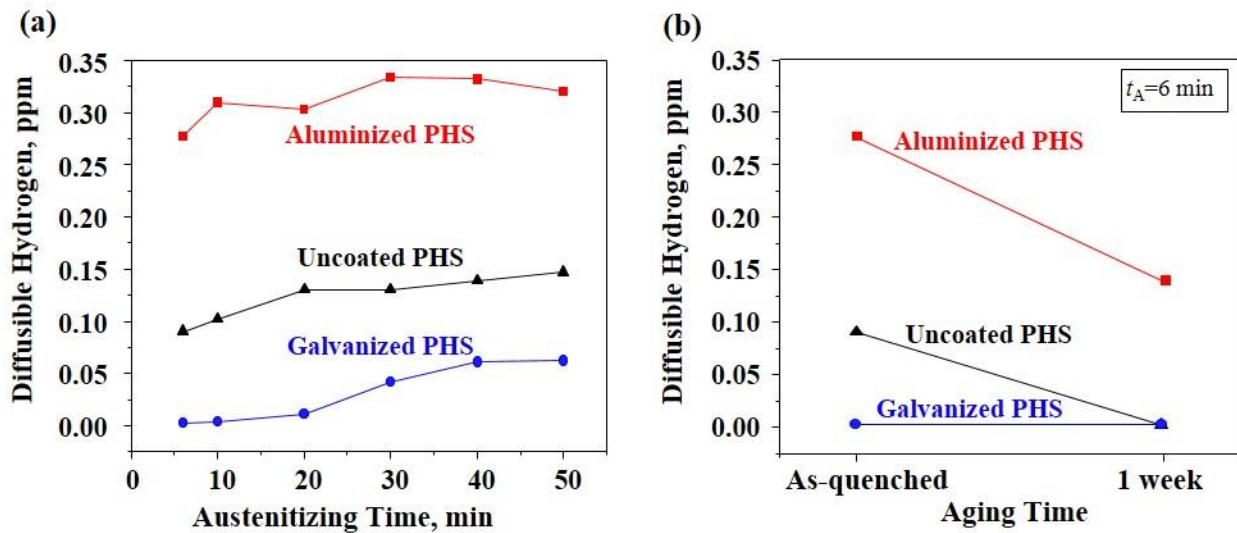


Fig. 5(a) TDA results of the diffusible hydrogen contents of the PHSs, austenitized at 900 °C for an austenitizing time ( $t_A$ ) in the range of 6-50 min and die-quenched to room temperature. (b) Changes in the diffusible hydrogen contents of the PHSs after aging at room temperature for one week.

### **3.3 Influence of hydrogen and coating type on the mechanical and fracture behavior**

The PHSs investigated in the present study, when not degraded by hydrogen embrittlement, had a 0.2 % offset yield strength (YS) of 1350 MPa, an UTS of 2000 MPa, and a total elongation (TE) of 5.5-7.0 %. Figures 6(a) to (c) show the tensile test results for uncoated, aluminized, and galvanized PHSs immediately after the HPF simulation (see also table 1). Three tensile tests were evaluated for each condition. The tensile properties, both the strength and ductility, were significantly influenced by the surface status or the content of the diffusible hydrogen of the specimens. The uncoated PHS specimens ruptured in the early stages of tensile straining. No post uniform elongation was observed, implying that these specimens fractured due to hydrogen embrittlement. The aluminized PHS specimens also fractured without post uniform elongation. The hydrogen-induced degradation of the mechanical properties was more severe for the aluminized PHS as compared to the uncoated PHS. This high sensitivity of the aluminized PHS to the hydrogen embrittlement is consistent with the highest diffusible hydrogen content of the aluminized PHS specimen (figures 4 and 5(a)). The galvanized PHS was much less susceptible to hydrogen uptake and the resultant hydrogen embrittlement. The galvanized PHS specimens exhibited normal tensile properties, a YS of 1380 MPa, a UTS of 2046 MPa, and a TE of 6.27 % all in average. Overall, the tensile test results shown in figure 6 indicate that the UTS and TE depended strongly on the surface status or diffusible hydrogen content, while the YS were nearly constant. In other words, the observed hydrogen-induced fracture generally occurred beyond the yield point.

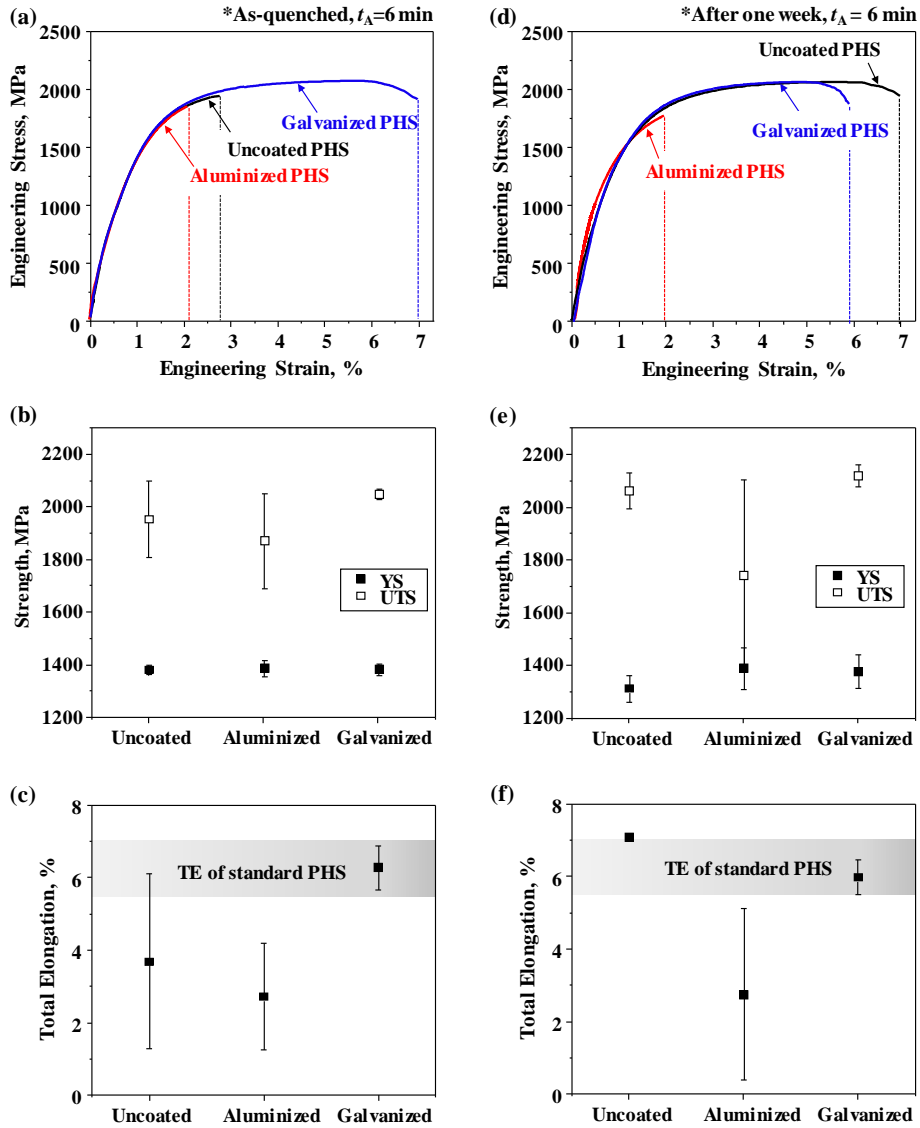


Fig. 6 Room temperature tensile properties of the uncoated, aluminized, and galvanized PHSs in the as-quenched state, i.e. immediately after the HPF simulation ((a) to (c)), and after aging at room temperature for one week ((d) to (f)). (a,d) Representative engineering stress-strain curves. (b,e) 0.2% offset yield strength (YS) and ultimate tensile strength (UTS). (c,f) Total elongation (TE). In all cases, the specimens were austenitized at 900 °C for 6 min and die-quenched to room temperature. The tensile tests were performed at a strain rate of  $5 \times 10^{-3} \text{ s}^{-1}$ . Error bars in (b), (c), (e), and (f) represent the standard deviation for three replicate tests per conditions. The light gray bands in (c) and (f) indicate a typical range for the TE of the standard PHS grade.

Table 1. Tensile properties of the PHSs in the as-quenched state. The reported results are averages and standard deviations of three repeated tests for each condition. In the current study, the brittle fracture stress was considered to be equivalent to the UTS.

	YS (MPa)	UTS (MPa)	TE (%)
Uncoated PHS	1379 ± 19	1950 ± 145	3.68 ± 2.42
Aluminized PHS	1384 ± 31	1868 ± 180	2.71 ± 1.46
Galvanized PHS	1380 ± 23	2046 ± 21	6.27 ± 0.60

Hydrogen embrittlement is a time-dependent temporary degradation phenomenon. The mechanical properties of the steel are recovered over time, as the diffusible hydrogen escape from the specimen. This recovery of the mechanical properties was, however, not observed for the aluminized PHS specimens. Figures 6(d) to (f) compare the tensile test results after the room temperature aging for one week (see also table 2). The tensile elongation of the uncoated specimens increased after the aging, and the uncoated specimens displayed a normal tensile behavior. This improvement of the plasticity is clearly associated with the release of the diffusible hydrogen during the room temperature aging (Figure 5(b)). The aluminized specimens aged for one week still fractured without post uniform elongation. The galvanized PHS exhibited normal tensile properties after the aging treatment.

Another indication that the hydrogen embrittlement observed in the present study was a time-dependent phenomenon is shown in figure 7. Since the hydrogen diffusion is temperature- and time-dependent, the degree of hydrogen-embrittlement susceptibility is expected to be strain-rate dependent [32, 33]. Figure 7 shows engineering stress-strain curves for the aluminized PHS in the as-quenched state, deformed at different strain rates. The hydrogen-induced loss in ductility was more significant when the aluminized PHS was tested at lower strain rates. The strain-rate dependence of the severity of the hydrogen effect on the mechanical properties of metals has been explained in connection with an interaction between hydrogen and dislocations. Sufficiently low strain rates can allow the hydrogen atoms to interact with moving dislocations, leading to the promotion of hydrogen embrittlement [33].

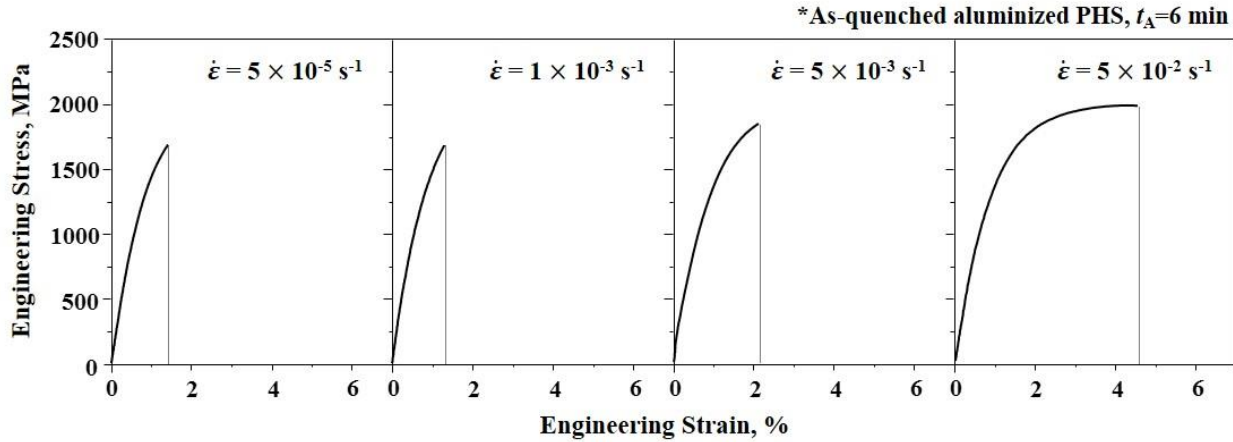


Fig. 7 Strain rate ( $\dot{\epsilon}$ )-dependent tensile properties of the aluminized PHS in the as-quenched state, i.e. immediately after the HPF simulation. In all cases, the aluminized specimens were austenitized at 900 °C for 6 min and die-quenched to room temperature.

Table 2. Tensile properties of the PHSs after aging at room temperature for one week. The reported results are averages and standard deviations of three repeated tests for each condition.

	YS (MPa)	UTS (MPa)	TE (%)
Uncoated PHS	1312 ± 50	2062 ± 67	7.09 ± 0.05
Aluminized PHS	1389 ± 79	1741 ± 362	2.74 ± 2.37
Galvanized PHS	1377 ± 62	2120 ± 42	5.97 ± 0.49

The fracture surface morphology of the PHS specimens depended on the coating type and the diffusible hydrogen content. Figure 8 shows optical micrographs of the fracture surface of the PHS specimens tensile-tested immediately after the HPF simulation. A flat fracture region, where the fracture plane was perpendicular to the loading axis, is visible on the fracture surface of both the uncoated and aluminized PHS specimens (figures 8(a) and (b)). The flat fracture regions are most likely hydrogen-induced, according to previous studies [34, 35]. The flat fracture area for the aluminized PHS specimen was larger than the uncoated PHS specimen, which is consistent with the higher hydrogen content in the aluminized PHS specimen (figure 4(a)). The galvanized PHS specimen, on the other hand, exhibited a shear-type fracture with a fracture angle of 62°, and an insignificant portion of the flat fracture region (figure 8(c)). Figure 9 shows SEM micrographs of the fracture surface. The flat fracture region of the uncoated PHS specimen was composed of

“quasi-cleavage” facets (figure 9(a)), characterized by small cleavage facets and fine tear ridges, and intergranular facets (figure 9(b)) as well as dimples (figures 9(a) and (b)). The slant fracture region, i.e. outside of the flat fracture region, was composed entirely of dimples, i.e. ductile microvoid coalescence features (figure 9(c)). Similarly, “quasi-cleavage” feature, intergranular facets, and dimples were observed in the flat fracture region of the aluminized PHS specimen (figures 9(d) and (e)), while the slant fracture region displayed fully dimpled fracture surface appearance (figure 9(f)). In addition, multiple hydrogen-induced cracks were present at the fracture surface of the aluminized PHS specimen (figure 9(d)). The observed “quasi-cleavage” and intergranular fracture features indicate that the sudden, premature failure noted for both the uncoated and aluminized PHS specimens in the as-quenched state (figures 6(a) and (d)) was due to the hydrogen-induced brittle fracture. The galvanized PHS had a completely dimpled fracture surface (figures 9(g) and (h)). No evidence for the hydrogen-induced brittle fracture such as “quasi-cleavage” facets and intergranular cracking was observed for the galvanized PHS, which did not contain diffusible hydrogen.

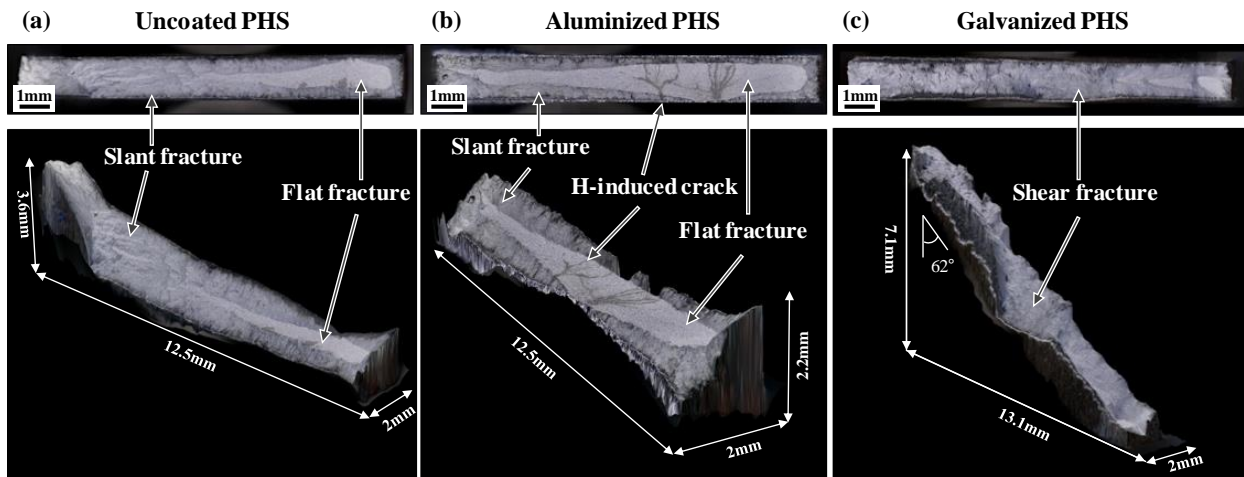


Fig. 8 In-focus (top) and 3D optical micrographs (bottom) of the fracture surface of tensile specimens in the as-quenched state. (a) Uncoated PHS. (b) Aluminized PHS. (c) Galvanized PHS. In all cases, the specimens were austenitized at 900 °C for 6 min prior to the die-quenching.

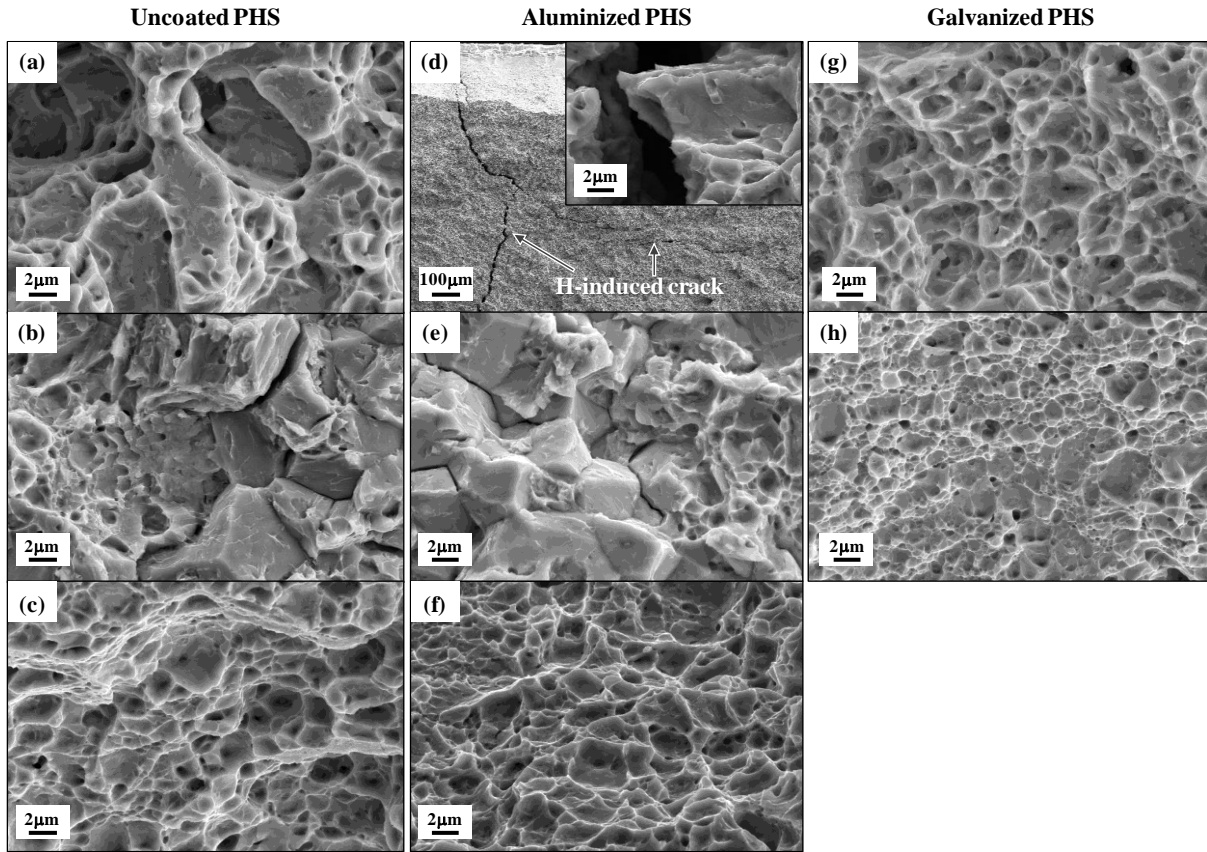
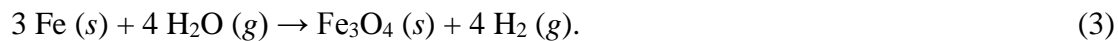
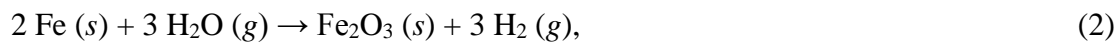


Fig. 9 SEM micrographs of the fracture surface of tensile specimens of uncoated PHS ((a) to (c)), aluminized PHS ((d) to (f)), galvanized PHS ((g) and (h)) in the as-quenched state. The specimens were austenitized at 900 °C for 6 min prior to the die-quenching.

### 3.4 Coating-type dependent hydrogen absorption and desorption mechanism

The hydrogen uptake of the PHSs reported herein is, regardless of the coating type or surface status, due to the high-temperature atmospheric corrosion process, i.e. water vapor reduction reaction by a metal. The hydrogen source is water vapor molecules in the atmosphere of the austenitization furnace. The hydrolysis of the metal (M) can generate hydrogen and the corresponding metal oxide ( $M_xO_y$ ) by the following reaction:  $xM + yH_2O \rightarrow M_xO_y + yH_2$  [36]. This hydrolysis reaction takes place during the austenitization of PHS [7]. The produced hydrogen molecules may be dissociated into hydrogen atoms at the metal surface and transported to the steel matrix.

The schematics of figure 10 illustrate the mechanisms of the hydrogen absorption of uncoated and coated PHSs during austenitization stage in the HPF process. After a continuous annealing process, the steel microstructure consists of ferrite and pearlite. When the HPF is applied to an uncoated steel (figure 10(a)),  $H_2O$  molecules in the furnace atmosphere react with Fe atoms at the steel surface to form Fe oxides and hydrogen atoms or molecules during the austenitization treatment [7]. The following reactions are thermodynamically possible in the furnace [10]:



The atomic hydrogen produced at the surface is then transferred to the steel matrix during the austenitization. At the same time, the austenitization treatment leads to the decarburization of the PHS surface. The austenitized steel is subsequently cooled to room temperature by press forming between water-cooled quenching dies. During the cooling, the austenitized steel transforms to  $\alpha'$ -martensite. The Fe oxide layer formed on the steel surface during the austenitization is removed by the shot blasting used in commercial practice. The hydrogen atoms trapped in the martensite naturally escape from the PHS at room temperature.

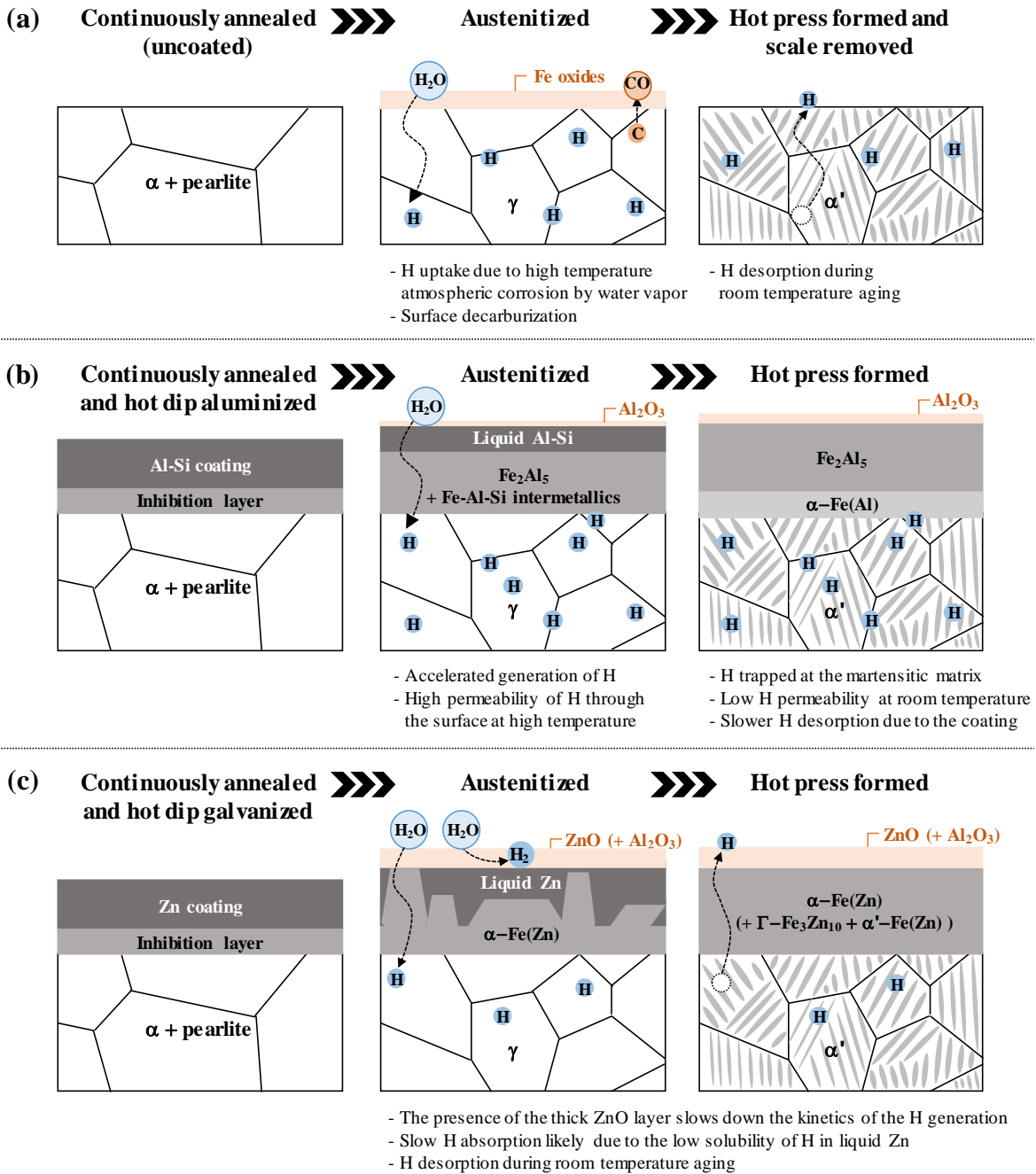


Fig. 10 Schematics illustrating the mechanisms of hydrogen absorption in (a) the uncoated PHS, (b) aluminized PHS, and (c) galvanized PHS during the HPF process. The hydrolysis of the metal (M) during the austenitization in HPF process generates  $H_2$  and the corresponding metal oxide ( $M_xO_y$ ) by the following reaction:  $xM + yH_2O \rightarrow M_xO_y + yH_2$ .  $\alpha$ ,  $\gamma$ , and  $\alpha'$  represent ferrite, austenite, and  $\alpha'$ -martensite, respectively.

The evolution of coating microstructure during the HPF process of coated PHSs has been reported in previous studies [18, 37]. During the heating and austenitization stage in the HPF process of an aluminized PHS (figure 10(b)), the Al-Si coating becomes partly liquid at approximately 660 °C. In the later stage of the austenitization, the reacted coating transforms entirely to a solid layer comprising various Fe-Al and Fe-Al-Si intermetallic phases [18]. In addition to the complex chemical reactions near the surface, hydrogen generation is accelerated due to the Al in the coating, by the following reaction [7]:  $2 \text{ Al } (l) + 3 \text{ H}_2\text{O } (g) \rightarrow \text{ Al}_2\text{O}_3 (s) + 3 \text{ H}_2 (g)$ . This reaction is known to efficiently produce a large amount of hydrogen [38]. Due to the excellent activity of Al to water, Al and Al-alloys have been used as superior materials for hydrogen generation [38]. Some of the hydrogen produced at the surface can be transported through the Al oxide layer in the form of ions ( $\text{H}^+$ ) and form hydrogen atoms beneath the layer [39]. Then, the hydrogen atoms can easily be transferred to the steel because of the high hydrogen permeability through liquid Al at the elevated temperature. The hydrogen solubility in liquid Al is around  $8 \times 10^{-3}$  at.-% in the temperature range of austenitization, i.e. 900 °C [25]. The diffusion of hydrogen in liquid Al ( $1.82 \times 10^{-7} \text{ m}^2/\text{s}$  [40]) is much faster than that in austenite at 900 °C ( $2.02 \times 10^{-8} \text{ m}^2/\text{s}$  [41]). The Al-rich coating, thus, provides a fast diffusion path for hydrogen from the surface to the austenite. On the other hand, a thin Al oxide layer that forms and grows at the coating surface reduces the rate of the reaction between Al and water [42], which slows down the hydrogen generation in the later stage of the austenitization (figure 5(a)). After the die quenching, the reacted coating layer acts as a very effective diffusion barrier and prevents hydrogen desorption from the lath martensite because the hydrogen solubility in the Al-rich coating is negligible at room temperature [25]. The mechanism for the hydrogen uptake of the aluminized PHS, in particular the effects of the Fe-Al intermetallics, was discussed in detail in a previous study [10].

While it is clear that Al in the coating plays an important role in the hydrogen absorption and desorption of Al-Si coated PHS, there is a remaining question as to the location of the hydrogen atoms trapped in the coated PHSs. To address this question, TDA was performed on PHS specimens after mechanical removal of the coating layer (Supplementary Materials). The diffusible hydrogen content of the aluminized PHS specimen in the as-quenched state was 0.28 ppm while the coating-stripped PHS specimen had a diffusible hydrogen content of 0.21-0.25 ppm

(Supplementary Table S1), i.e. the coating removal resulted in only a slight decrease of the diffusible hydrogen content. The fact that the diffusible hydrogen contents of the aluminized PHS specimen and coating-stripped PHS specimen were comparable implies that most of the diffusible hydrogen atoms were trapped in the martensitic matrix, rather than in the reacted coating layer.

During the austenitization treatment of a galvanized PHS (figure 10(c)), the pure Zn coating layer is liquified above 420 °C. At the same time, the coating surface is oxidized by the water vapor and gaseous oxygen in the furnace atmosphere. Therefore, the coating microstructure near the surface is composed of the Fe-saturated liquid Zn and solid ZnO layers in the initial stage of the austenitization. Subsequently, the liquid Zn is replaced entirely with the solid  $\Gamma$ -Fe<sub>3</sub>Zn<sub>10</sub> and  $\alpha$ -Fe(Zn) phases. In principle, the reaction between the Zn coating and water, i.e.  $\text{Zn} (l) + \text{H}_2\text{O} (g) \rightarrow \text{ZnO} (s) + \text{H}_2 (g)$ , should also generate hydrogen [43]. The moisture-induced hydrogen uptake can also take place during the austenitization of a galvanized PHS (figure 10(c)). There are, however, several mechanisms that may cause the slow kinetics of hydrogen absorption of the galvanized PHS (figures 4(d) and 5(a)). The hydrogen productivity by the Zn hydrolysis is, in theory, lower compared to those of Al and Fe because of the high molecular weight and relatively low valence of Zn [36] (Table 3). Moreover, the formation of the Zn oxide layer, which grows and thickens much more rapidly compared to the Al oxide layer on the aluminized PHS (figures 2 and 3), can substantially slow down the kinetics of the reaction between Zn and water vapor during the austenitization. Berman and Epstein [43] studied the kinetics of hydrogen production in the oxidation of liquid Zn by water vapor. They reported that transport of Zn through the solid ZnO layer on the liquid Zn was the rate-determining stage of the hydrogen generation [43]. In addition to the slow generation of hydrogen, transport of the produced hydrogen through the liquid Zn is expected to be very slow since the hydrogen solubility in the liquid Zn is considerably small. The solubility of hydrogen in liquid Zn at a temperature close to the melting point is two orders of magnitude smaller than for liquid Al [44] ( $1 \times 10^{-5}$  at.-% hydrogen at 516 °C for liquid Zn [45] and  $2 \times 10^{-3}$  at.-% hydrogen at 660 °C for liquid Al [25]). Accordingly, the very small solubility of liquid Zn prevents the hydrogen uptake of the galvanized PHS in the initial stage of the austenitization (figures 4(d) and 5(a)). Furthermore, the reacted coating layer of the galvanized PHS, comprising mostly  $\alpha$ -Fe(Zn), i.e. Zn-containing ferrite, has no significant influence on the

hydrogen desorption at room temperature [29]. Therefore, after the die quenching, even a small amount of the diffusible hydrogen absorbed in the galvanized PHS can easily out-diffuse through the reacted coating layer. This suggests that applying Zn-based coatings may be one approach to lowering the hydrogen uptake and mitigating the resulting hydrogen embrittlement of ultra-high strength PHSs.

Table 3. Theoretical hydrogen productivity of different hydrolysis reactions [37].

Reaction	Mole H <sub>2</sub> per 1 gram of metal	Metal oxide per mole H <sub>2</sub> (gram)
$2 \text{ Al} + 3 \text{ H}_2\text{O} \rightarrow \text{Al}_2\text{O}_3 + 3 \text{ H}_2$	0.056	33.99
$\text{Fe} + \text{H}_2\text{O} \rightarrow \text{FeO} + \text{H}_2$	0.018	71.85
$\text{Zn} + \text{H}_2\text{O} \rightarrow \text{ZnO} + \text{H}_2$	0.015	81.41

## 4 Conclusions

The sensitivity of uncoated, aluminized, and galvanized PHSs to hydrogen uptake during the HPF process and the resultant embrittlement was investigated by means of TDA and uni-axial tensile tests. The main conclusions of the present study are as follows:

1. A small amount of diffusible hydrogen was introduced into the uncoated PHS during HPF. It resulted in the degradation of the mechanical properties, which was transient, since most of the diffusible hydrogen escaped from the steel in a week.
2. The Al-10%Si coating was found to promote the absorption of diffusible hydrogen at elevated temperature during HPF. The hydrogen absorbed in the aluminized PHS was trapped mostly in the martensitic matrix, rather than in the reacted coating layer. The reacted coating layer, composed mostly of Fe-Al and Fe-Al-Si intermetallics, prevented the absorbed hydrogen from out-diffusing through the reacted coating surface layer at room temperature. This caused the persistence of the sensitivity of the aluminized PHS to hydrogen-induced brittle fracture and the very slow recovery of the mechanical properties. The resulting hydrogen embrittlement was substantially more pronounced during tensile tests at low strain rates.
3. The possibility of using a Zn coating to mitigate the hydrogen uptake and embrittlement of ultra-high strength PHS seems promising, because the Zn coating on the galvanized PHS effectively prevented hydrogen uptake during the HPF process, and no evidence of hydrogen-induced brittle fracture was observed for the galvanized PHS. The greater embrittlement resistance of the galvanized PHS is attributed to both the inhibition of the hydrogen generation reaction by the surface ZnO oxide layer and the low rate of hydrogen transport through the liquid Zn phase.

## Acknowledgments

The authors gratefully acknowledge the partial support of the POSCO Technical Research Laboratories, Gwangyang, South Korea.

## Data Availability Statement

The raw/processed data required to reproduce these findings cannot be shared at this time due to technical or time limitations.

## References

- [1] H. Karbasian, A.E. Tekkaya, A review on hot stamping, *Journal of Materials Processing Technology* 210(15) (2010) 2103-2118.
- [2] K. Mori, P. Bariani, B.-A. Behrens, A. Brosius, S. Bruschi, T. Maeno, M. Merklein, J. Yanagimoto, Hot stamping of ultra-high strength steel parts, *CIRP Annals* 66(2) (2017) 755-777.
- [3] C. Allély, L. Dosdat, O. Clauzeau, K. Ogle, P. Volovitch, Anticorrosion mechanisms of aluminized steel for hot stamping, *Surface and Coatings Technology* 238 (2014) 188-196.
- [4] R. Autengruber, G. Luckeneder, A.W. Hassel, Corrosion of press-hardened galvanized steel, *Corrosion Science* 63 (2012) 12-19.
- [5] D.W. Fan, B.C. De Cooman, State-of-the-Knowledge on Coating Systems for Hot Stamped Parts, *Steel Research International* 83(5) (2012) 412-433.
- [6] L. Cho, H. Kang, C. Lee, B.C. De Cooman, Microstructure of liquid metal embrittlement cracks on Zn-coated 22MnB5 press-hardened steel, *Scripta Materialia* 90 (2014) 25-28.
- [7] C. Georges, T. Sturel, P. Drillet, J.-M. Mategne, Absorption/desorption of diffusible hydrogen in aluminized boron steel, *ISIJ international* 53(8) (2013) 1295-1304.
- [8] O. Schwedler, M. Zinke, S. Jüttner, Determination of hydrogen input in welded joints of press-hardened 22MnB5 steel, *Welding in the World* 58(3) (2014) 339-346.
- [9] R. Scharf, A. Muhr, G. Luckeneder, P. Larour, K. Mraczek, J. Rehrl, F. Leomann, K.H. Stellnberger, J. Faderl, G. Mori, Hydrogen embrittlement of DP-1000 flat steel sheet: Influence of

- mechanical properties, specimen geometry, pre-damaging and electrolytically zinc galvanizing, *Materials and Corrosion* 67(3) (2016) 239-250.
- [10] L. Cho, D.H. Sulistiyo, E.J. Seo, K.R. Jo, S.W. Kim, J.K. Oh, Y.R. Cho, B.C. De Cooman, Hydrogen absorption and embrittlement of ultra-high strength aluminized press hardening steel, *Materials Science and Engineering: A* 734 (2018) 416-426.
- [11] L. Cho, E.J. Seo, D.H. Sulistiyo, K.R. Jo, S.W. Kim, J.K. Oh, Y.R. Cho, B.C. De Cooman, Influence of vanadium on the hydrogen embrittlement of aluminized ultra-high strength press hardening steel, *Materials Science and Engineering: A* 735 (2018) 448-455.
- [12] C. Heneger, Hydrogen permeation barrier coatings, *Materials for the Hydrogen Economy*, CRC Press Taylor & Francis Group Boca Raton, FL2008.
- [13] H.-H. Jeon, S.-M. Lee, J. Han, I.-J. Park, Y.-K. Lee, The effect of Zn coating layers on the hydrogen embrittlement of hot-dip galvanized twinning-induced plasticity steel, *Corrosion Science* 111 (2016) 267-274.
- [14] D.H. Coleman, B.N. Popov, R.E. White, Hydrogen permeation inhibition by thin layer Zn–Ni alloy electrodeposition, *Journal of Applied Electrochemistry* 28(9) (1998) 889-894.
- [15] H. Kamoutsi, G. Haidemenopoulos, V. Bontozoglou, S. Pantelakis, Corrosion-induced hydrogen embrittlement in aluminum alloy 2024, *Corrosion Science* 48(5) (2006) 1209-1224.
- [16] J.-K. Lee, Kinetics of hydrogen movement in zinc, *Journal of Korean Physical Society* 51 (2007) 1320.
- [17] J. Bian, H. Lu, W. Wang, Impact of alloying design on the crash relevant Material Properties of press hardening steel based on Mn-B concept, *Advanced High Strength Steel and Press Hardening: Proceedings of the 2nd International Conference on Advanced High Strength Steel and Press Hardening (ICHSU 2015)*, World Scientific, 2016, pp. 20-26.
- [18] M. Windmann, A. Röttger, W. Theisen, Phase formation at the interface between a Boron Alloyed Steel substrate and an Al-rich coating, *Surface and Coatings Technology* 226 (2013) 130-139.
- [19] A. Mignone, S. Frangini, A. La Barbera, O. Tassa, High temperature corrosion of B2 iron aluminides, *Corrosion Science* 40(8) (1998) 1331-1347.

- [20] C.W. Lee, D.W. Fan, I.R. Sohn, S.-J. Lee, B.C. De Cooman, Liquid-metal-induced embrittlement of Zn-coated hot stamping steel, *Metallurgical and Materials Transactions A* 43(13) (2012) 5122-5127.
- [21] N.L. Okamoto, D. Kashioka, M. Inomoto, H. Inui, H. Takebayashi, S. Yamaguchi, Compression deformability of  $\Gamma$  and  $\zeta$  Fe–Zn intermetallics to mitigate detachment of brittle intermetallic coating of galvanized steels, *Scripta Materialia* 69(4) (2013) 307-310.
- [22] C.W. Lee, W.S. Choi, Y.R. Cho, B.C. De Cooman, Surface oxide formation during rapid heating of Zn-coated press hardening steel, *ISIJ International* 54(10) (2014) 2364-2368.
- [23] Y. Liu, X. Chong, Y. Jiang, R. Zhou, J. Feng, Mechanical properties and electronic structures of Fe-Al intermetallic, *Physica B: Condensed Matter* 506 (2017) 1-11.
- [24] V. Bhavsar, T.S. Dang, H. Patel, B. Rehani, N. Jamnapara, Structural characterization of aluminized steel heat treated in different environments, *Surface and Coatings Technology* 335 (2018) 88-94.
- [25] C. Qiu, G.B. Olson, S.M. Opalka, D.L. Anton, Thermodynamic evaluation of the Al-H system, *Journal of Phase Equilibria and Diffusion* 25(6) (2004) 520-527.
- [26] H.K.D.H. Bhadeshia, Prevention of hydrogen embrittlement in steels, *ISIJ international* 56(1) (2016) 24-36.
- [27] M. Wang, E. Akiyama, K. Tsuzaki, Hydrogen degradation of a boron-bearing steel with 1050 and 1300MPa strength levels, *Scripta Materialia* 52(5) (2005) 403-408.
- [28] A.-M. Brass, F. Guillon, S. Vivet, Quantification of hydrogen diffusion and trapping in 2.25 Cr-1Mo and 3Cr-1Mo-V steels with the electrochemical permeation technique and melt extractions, *Metallurgical and Materials Transactions A* 35(5) (2004) 1449-1464.
- [29] M. Kuhlmann, O. Schwedler, N. Holtschke, S. Jüttner, Consideration of hydrogen transport in press-hardened 22MnB5, *Materials Testing* 57(11-12) (2015) 977-984.
- [30] G. Hollenberg, E. Simonen, G. Kalinin, A. Terlain, Tritium/hydrogen barrier development, *Fusion Engineering and Design* 28 (1995) 190-208.
- [31] K. Forcey, D. Ross, C. Wu, The formation of hydrogen permeation barriers on steels by aluminising, *Journal of Nuclear Materials* 182 (1991) 36-51.

- [32] Y. Momotani, A. Shibata, D. Terada, N. Tsuji, Effect of strain rate on hydrogen embrittlement in low-carbon martensitic steel, *International Journal of Hydrogen Energy* 42(5) (2017) 3371-3379.
- [33] C. Hwang, I. Bernstein, Dislocation transport of hydrogen in iron single crystals, *Acta Metallurgica* 34(6) (1986) 1001-1010.
- [34] T. Doshida, H. Suzuki, K. Takai, N. Oshima, T. Hirade, Enhanced lattice defect formation associated with hydrogen and hydrogen embrittlement under elastic stress of a tempered martensitic steel, *ISIJ International* 52(2) (2012) 198-207.
- [35] T. Doshida, M. Nakamura, H. Saito, T. Sawada, K. Takai, Hydrogen-enhanced lattice defect formation and hydrogen embrittlement of cyclically prestressed tempered martensitic steel, *Acta Materialia* 61(20) (2013) 7755-7766.
- [36] I. Vishnevetsky, M. Epstein, Production of hydrogen from solar zinc in steam atmosphere, *International Journal of Hydrogen Energy* 32(14) (2007) 2791-2802.
- [37] R. Autengruber, G. Luckeneder, S. Kolnberger, J. Faderl, A.W. Hassel, Surface and Coating Analysis of Press-Hardened Hot-Dip Galvanized Steel Sheet, *Steel Research International* 83(11) (2012) 1005-1011.
- [38] K. Mahmoodi, B. Alinejad, Enhancement of hydrogen generation rate in reaction of aluminum with water, *International Journal of Hydrogen Energy* 35(11) (2010) 5227-5232.
- [39] J. Draley, W. Ruther, Some unusual effects of hydrogen in corrosion reactions, *Journal of The Electrochemical Society* 104(6) (1957) 329-333.
- [40] N. Jakse, A. Pasturel, Hydrogen diffusion in liquid aluminum from ab initio molecular dynamics, *Physical Review B* 89(17) (2014) 174302.
- [41] J. Fast, Gases in Metals, Philips Technical Library, Macmillan, 1976.
- [42] J.T. Ziebarth, J.M. Woodall, R.A. Kramer, G. Choi, Liquid phase-enabled reaction of Al–Ga and Al–Ga–In–Sn alloys with water, *International Journal of Hydrogen Energy* 36(9) (2011) 5271-5279.
- [43] A. Berman, M. Epstein, The kinetics of hydrogen production in the oxidation of liquid zinc with water vapor, *International Journal of Hydrogen Energy* 25(10) (2000) 957-967.
- [44] A. Rack, A. Haibel, B. Matijasevic, J. Banhart, Synchrotron tomography on zinc and aluminium foams, J. Banhart, Cellular metals: manufacture, properties, applications. International

Conference on Cellular Metals and Metal Foaming Technology, Berlin, MetFoam, Berlin: Verl. MIT Publ, 2003, pp. 295-300.

[45] W. Hofmann, J. Maatsch, The problem of gas solubility in nonferrous metals, *Neue Huette* 2 (1957) 648-50.

## Supplementary Materials

### Effects of Al-Si Coating and Zn Coating on the Hydrogen Uptake and Embrittlement of Ultra-High Strength Press-Hardened Steel

Kyoung Rae Jo<sup>a</sup>, Lawrence Cho<sup>a,b,\*</sup>, Dimas H. Sulistiyono<sup>a</sup>, Eun Jung Seo<sup>a,c</sup>,  
Seong Woo Kim<sup>d</sup>, Bruno C. De Cooman<sup>a,†</sup>

<sup>a</sup>Graduate Institute of Ferrous Technology, Pohang University of Science and Technology,  
Pohang, 37673, South Korea

<sup>b</sup>National Institute of Standards and Technology, Boulder, CO 80305, USA

<sup>c</sup>Advanced Steel Processing and Products Research Center,  
Colorado School of Mines, Golden, CO 80401, USA

<sup>d</sup>Technical Research Laboratories, POSCO, Gwangyang, 57807, South Korea

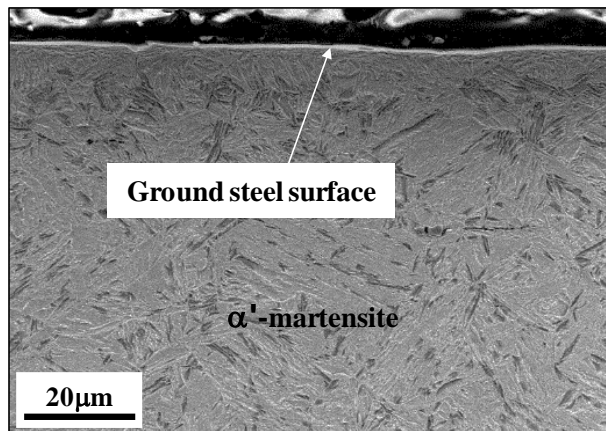
<sup>†</sup>Deceased August 29, 2018.

\*Corresponding author. Tel: +1-303-497-6853. Email: [lawrence.cho@nist.gov](mailto:lawrence.cho@nist.gov)

For the hot press forming (HPF) simulation, aluminized steel specimens were austenitized at 900 °C for 6 min and die-quenched to room temperature. Thermal desorption analysis (TDA) of the aluminized press hardened steel (PHS) specimen was done immediately after the HPF. In the case of the coating-stripped specimens, both sides of the surface of the aluminized PHS specimens were mechanically ground with 400-grit SiC paper prior to the TDA. No coolant was used in the grinding process in order to avoid an interaction of the specimens with water or moisture. Supplementary Fig. S1 shows a cross-sectional scanning electron microscopy (SEM) image of the surface and subsurface microstructure of the coating-stripped PHS specimen, indicating an entire removal of the reacted coating layer.

The TDA was performed using a diffusible hydrogen analyzer equipped with a thermal conductivity detector. The hydrogen desorption rate for the aluminized and coating-stripped PHS specimens was measured during heating from 50 °C to 400 °C using a heating rate of 20 °C/min. In the present study, the diffusible hydrogen was defined as the hydrogen that desorbs at low temperature. It corresponds to the hydrogen atoms which give rise to the first desorption rate peak appearing in the 100-400 °C temperature range in the TDA curves. In the case of the coating-stripped condition, the TDA was performed for two specimens.

Supplementary Table S1 compares the contents of the diffusible hydrogen of the aluminized PHS specimen and coating-stripped PHS specimens. The diffusible hydrogen content of the aluminized PHS specimen was 0.28 ppm. The diffusible hydrogen content of the coating-stripped PHS specimen was 0.21-0.25 ppm. The coating removal resulted in only a slight decrease of the diffusible hydrogen content. The fact that the difference in the diffusible hydrogen content between the aluminized and coating-stripped specimens was small indicates that most of the diffusible hydrogen atoms in the aluminized PHS are trapped at the martensitic matrix, rather than in the reacted coating layer.



Supplementary Fig. S1 Cross-sectional SEM micrograph of the ground surface of an aluminized PHS specimen, austenitized at 900 °C for 6 min and die-quenched to room temperature.

Supplementary Table S1 Hydrogen-thermal desorption analysis (TDA) results of the diffusible hydrogen contents of the aluminized press hardened steel (PHS) specimen and coating-stripped PHS specimen.

Diffusible hydrogen content		
Aluminized PHS specimen	First measurement	0.28 mass ppm
Coating-stripped PHS specimen	First measurement	0.21 mass ppm
	Second measurement	0.25 mass ppm